pISSN 2384-1095
eISSN 2384-1109

iMRI 2019;23:328-340

https://doi.org/10.13104/imri.2019.23.4.328

iMRI
Investigative Magnetic Resonance Imaging

Generating Motion- and Distortion-Free Local Field Map Using 3D Ultrashort TE MRI: Comparison with T_2* Mapping

Kyle Jeong[1,2], Bijaya Thapa[1,3], Bong-Soo Han[4], Daehong Kim[5], Eun-Kee Jeong[1,6]

[1]Utah Center for Advanced Imaging Research, University of Utah, Salt Lake City, UT, USA
[2]Department of Biomedical Engineering, University of Utah, Salt Lake City, UT, USA
[3]Department of Physics, University of Utah, Salt Lake City, UT, USA
[4]Radiology and Imaging Sciences, University of Utah, Salt Lake City, UT, USA
[5]Radiological Sciences, Yonsei University, Wonju, Korea
[6]Molecular Imaging & Therapy Branch, National Cancer Center, Goyang-si, Korea

Original Article

Received: November 10, 2018
Revised: February 9, 2019
Accepted: March 26, 2019

Correspondence to:
Eun-Kee Jeong, Ph.D.
Utah Center for Advanced Imaging Research Dept. of Radiology and Imaging Sciences
University of Utah, Salt Lake City, UT 84108, USA.
Tel. +1-801-581-8643
Fax. +1-801-585-3592
E-mail: ek.jeong@utah.edu

Purpose: To generate phase images with free of motion-induced artifact and susceptibility-induced distortion using 3D radial ultrashort TE (UTE) MRI.

Materials and Methods: The field map was theoretically derived by solving Laplace's equation with appropriate boundary conditions, and used to simulate the image distortion in conventional spin-warp MRI. Manufacturer's 3D radial imaging sequence was modified to acquire maximum number of radial spokes in a given time, by removing the spoiler gradient and sampling during both rampup and rampdown gradient. Spoke direction randomly jumps so that a readout gradient acts as a spoiling gradient for the previous spoke. The custom raw data was reconstructed using a homemade image reconstruction software, which is programmed using Python language. The method was applied to a phantom and *in-vivo* human brain and abdomen. The performance of UTE was compared with 3D GRE for phase mapping. Local phase mapping was compared with T_2* mapping using UTE.

Results: The phase map using UTE mimics true field-map, which was theoretically calculated, while that using 3D GRE revealed both motion-induced artifact and geometric distortion. Motion-free imaging is particularly crucial for application of phase mapping for abdomen MRI, which typically requires multiple breathold acquisitions. The air pockets, which are caught within the digestive pathway, induce spatially varying and large background field. T_2* map, that was calculated using UTE data, suffers from non-uniform T_2* value due to this background field, while does not appear in the local phase map of UTE data.

Conclusion: Phase map generated using UTE mimicked the true field map even when non-zero susceptibility objects were present. Phase map generated by 3D GRE did not accurately mimic the true field map when non-zero susceptibility objects were present due to the significant field distortion as theoretically calculated. Nonetheless, UTE allows for phase maps to be free of susceptibility-induced distortion without the use of any post-processing protocols.

Keywords: Ultrashort TE; UTE; Fieldmap; Phasemap; Quantitative susceptibility mapping; Susceptibility imaging

INTRODUCTION

Phase image of the MRI is used to generate a field map, which has been used to correct the geometric distortion, such as in EPI-type acquisition for fMRI and diffusion MRI, and to generate a local (tissue) field for susceptibility-weighted imaging (SWI) (1, 2) and quantitative susceptibility mapping (3, 4). T_2* mapping has long been used to quantitatively represent the change in field-inhomogeneity, such as in dynamic susceptibility contrast MRI (DSC) in stroke evaluation. However, it is dominated by the field inhomogeneity term $\gamma\Delta B_z$ (5-8), which it is difficult to be removed. As the main purpose of T_2* mapping is to extract the effect contributed by the local tissue field, not the background field, and the field inhomogeneity term $\gamma\Delta B_z$ includes the local field variation induced by both global (background) and local (tissue) influences, one desires to remove the background field variation, which is mainly induced by poor shimming, air/tissue and bone/tissue interfaces. Unlike in the T_2*, it is possible to remove the phase contribution from background field and, in principle, obtain only the local field term which is induced by the magnetic susceptibility of the local tissue.

Recently, susceptibility imaging, such as the quantitative susceptibility mapping (QSM), has been emerging to quantitatively map the local magnetic susceptibility. It is a promising approach to identify and quantify iron-based residues and gadolinium-based molecules that are of great interest, such as in liver (9, 10) and brain (4, 11). Yablonskiy et al. presented a biophysical mechanism of phase differences in brain (12, 13). Procedure for calculating a QSM starts from multi-echo phase images, includes removal of global background phase and field-to-source inversion on the local phase image (4, 11). Therefore, a robust phase map is crucial for successful QSM.

3D GRE is commonly used to generate the phase image for QSM. However, all conventional Fourier-Transform (FT) MRIs suffer from geometric distortion, which a pixel signal with off-resonance shifts toward to the direction with lower effective bandwidth, typically along the frequency-encoding direction (5, 6), except EPI-type acquisition of that distortion is along the phase-encoding direction (14). Because of this directional bias, the resultant fieldmap is very different from that of the real field distribution, particularly around the structure with large difference in the magnetic susceptibility.

In all conventional FT MRI using phase-encoding, physiological motion couples with the phase-encoding gradient and induces a pseudo-random phase-error into the raw data. This phase-error causes a ghosting artifact in the phase-encoding direction or local shading artifact. The GRE MRI often suffers from signal void at such location due to the short T_2*. The minimum TE of 3D GRE is typically in the order of few msec, which may be too long for a place with a large ΔBz. The phase value of these points, calculated from low SNR, will not be accurate. One needs to solve an inverse problem from a resultant tissue field to map the magnetic susceptibility. One problem with FT MRI is the motion-induced artifact, which the phase-encoding gradient couples with physiological motion and spread the signal along the phase-encoding direction. As a result, local field map will be corrupted.

In this report, 3D radial ultrashort-TE (UTE) MRI is used for robust phase and field mappings (15-17). Because there is no specific readout direction, the measured fieldmap deomstrates the actual field distribution, and also the TE can be as short as tens of us in modern clinical MRI system for UTE MRI, the resultant images show significantly reduced signal void, related to susceptibility-induced local field variation. Also, because UTE MRI acquires heavy sampling at k_o without utilizing the phase-encoding (5, 6), it is intrinsically free from any motion-induced ghost artifact, although the physiological motion tends to blur the resultant image along the motion direction. Using the theoretical field ditribution that is induced by a sphrical and cylindrical objects surrounded by water, we numerically simulate the anicipated field map.

MATERIALS AND METHODS

All MR imaging experiments were performed at a wholebody 3T MRI system (Tim-Trio, Siemens Medical Solutions, Erlangen, Germany), which is equipped with 40 mT/m gradient strength with 200 mT/m/s slewrate. A twelve-channel receive-only head RF coil was used for imaging of phantom and human brain, and combination of a torso and spine RF coils were used for abdominal imaging. All volunteers signed the institution approved consent forms. All human imagings were performed under the protocol approved by institutional review board, and signed consent was collected from all participating subjects.

Computer Simulation of Geometric Distortion in Conventional MRI

The local field induced by a uniform object with a

spherical or cylindrical symmetry with its magnetic susceptibility $\Delta\chi$ relative to its surrounding water, can be theoretically calculated using an electromagnetic theory. Here, the sign in the difference of the magnetic susceptibility $\Delta\chi$ determines the para- or dia-magnetism of the object relative to the surrounding tissue water.

The field induced by a solid sphere or a solid cylinder, running perpendicular to the external magnetic field B_o, are derived by solving a Laplace's equation $\nabla^2\Psi = 0$ for a static magnetic potential Ψ with an appropriate vector potential $\vec{A} = 0$, and applying appropriate boundary conditions (18-21). We assume that the magnetic field inside the surrounding water without the object is $B_o\hat{z}$. The z-components of the resultant fields are described as,

$$\Delta B_z(\vec{r}) = -B_o \frac{\Delta\chi}{3+\Delta\chi}\frac{R^3}{r^3}(1-3\cos^2\theta) = -B_o \frac{\Delta\chi}{3}\frac{R^3}{r^3}(1-3\cos^2\theta),$$

for a solid sphere ... [1]

$$\Delta B_z(\vec{r}) = -0.5B_o\Delta\chi\frac{R^2}{r^2}(\cos^2\theta-\sin^2\theta),$$ for an infinite solid cylinder ... [2]

Here, θ is the polar angle from the external magnetic field $\vec{B} = B_o\hat{z}$, $\Delta\chi = \chi_{in}-\chi_{out}$, R the radius of the sphere or cylinder.

Figure 1 illustrates the phase images of the current simulation. Local field maps are numerically simulated using eqs. [1, 2] and used to synthetically generate the phase images to simulate the geometric distortion for 3D radial and conventional non-radial MR imagings, which are shown in Figure 1a-d and Figure 1e-h, respectively. Simulation parameters are imaging field-of-view (FOV) = 128 × 128 × 128 mm^3, object radius of 6.4 mm, readout matrix of 512, $\Delta\chi$ = 16 ppm, and receiver bandwidth of 25 Hz/pixel.

CONSTRUCTION OF PHASE MAP

In pixel-by-pixel, the complex images of TE_1 are multiplied by the complex conjugate images of the TE_2, and the angle is calculated by taking the arctangent of the resultant complex number.

$$\Delta\emptyset(\vec{r}) = \angle\{\vec{M}(\vec{r};TE_2)\vec{M}^*(\vec{r};TE_1)\},$$ ... [3]

The phase image is unwrapped using unwrap_phase in scikit_image python module (22, 23). The method investigates and compares each pixel value of phase with its neighboring pixels and cautiously adds 2π to phase value

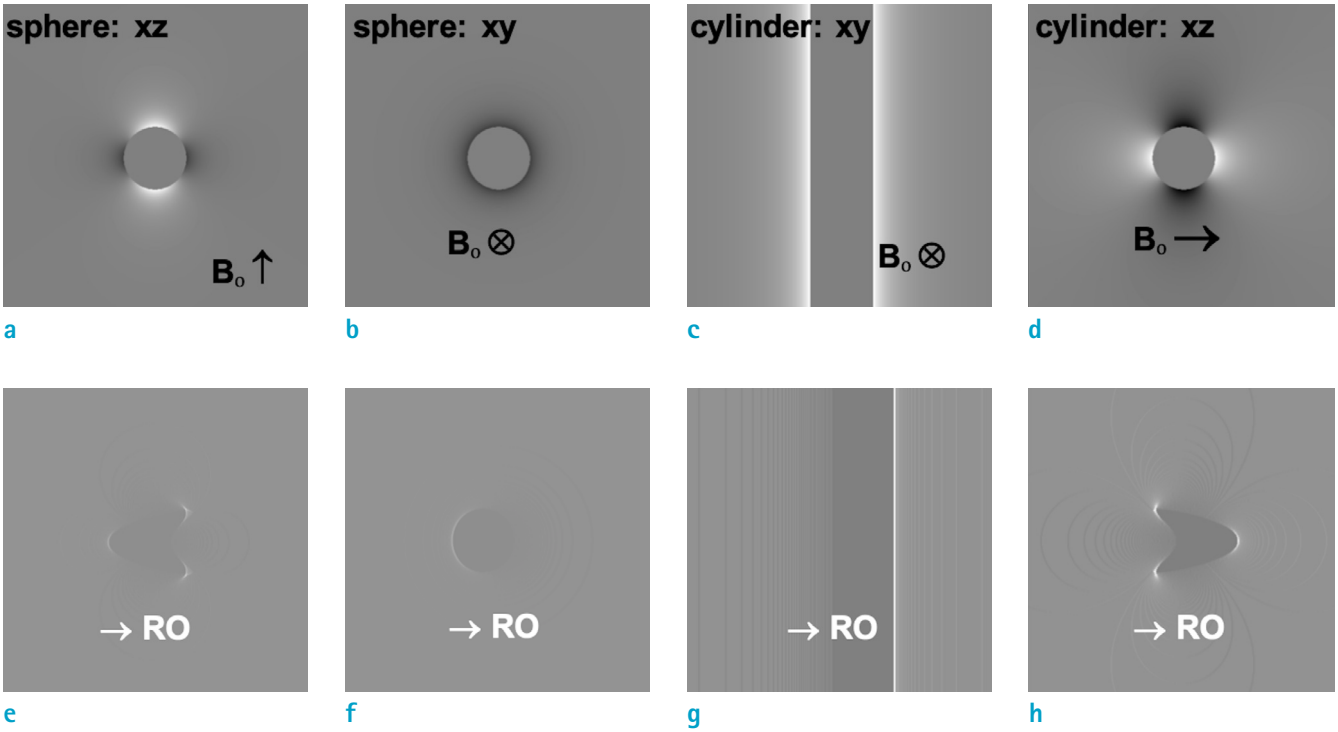

Fig. 1. Numerical simulation of (a-d: top row) local field variation and (e-h: bottom row) geometric distortion in the typical FT MRI images for (a, b, e, f). a solid sphere and (c, d, g, h). a solid cylinder with $\Delta\chi$ = +16 ppm. The cylinder in (c, d, g, h) is oriented perpendicular to the external static magnetic field B_o.

if the phase difference is greater than a set threshold phase value.

The measured phase of each voxel is a sum of background phase θ_L and local tissue phase θ_B. Because the local phase is of our interest, the background phase must be removed. One particular technique is to exploit the characteristics of phase image in the spatial-frequency domain. The local phase is of high spatial frequency while background phase is of low spatial frequency. Consequently, a high-pass filter (HPF) can be applied to the phase image in its spatial-frequency domain for the removal of background field. Hence, the combined and unwrapped phase image is convolved with a 15 × 15 × 15 Gaussian kernel in pixel-by-pixel to remove the high-frequency components, and this low-pass-filtered phase image is then subtracted from the unfiltered image, which results in a HPF local phase image [3].

The local phase or field map was used to construct a QSM using the inverse Fourier Transformation [3]. Threshold value of 2.0 was used to avoid the streaking artifact near the singular point along $F(\theta = 54.7°)$, which may appear with a large threshold value.

$$\chi(\vec{r}) = FT^{-1}\left[FT\left(\frac{\emptyset(\vec{r})}{-\gamma B_o T_E}\right)\cdot F \right] \text{ and}$$

$$F(\vec{k}) = \frac{3}{1-3(k_z/K)^2} = \frac{3}{1-3\cos^2\theta}, \quad \ldots [4]$$

where θ is the angle between $\vec{k}$ and $\hat{z}$ in k-space. The function $F(\vec{k})$ becomes singular at where the angle θ approaches to the magic angle 54.7°. Thus, $F(\vec{k})$ is set to 2/3 at $F(\vec{k}) \geq F_{th}$ (= 2/3) [4].

Pulse Sequence: To reduce the blurriness in the resultant images, the number of radial spokes needs to be maximized over increased number of averaging for a fixed acquisition time. First, the radial view angles are generated for the entire measurement using the kooshball type ordering by the manuscfacturer's algorithm, and then randomly shuffled using C++ function "random-shuffle". The number of radial spokes per a given imaging time is maximized by removing the spoiler gradient to shorten the minimum repetition time and using the randomly distributed radial spoke direction, of which the radial readout gradient plays as a spoiling gradient for the previous readout. For patient imaging, free-breathing acquisition is highly preferred, although it is likely that the position of the lung varies during the respiration cycle.

Manufacturer's pulse sequence was modified to improve the time efficiency of the data acquisition by removing the spoiler gradient after the data sampling (Figure 1). The second FID data was sampled with an identical readout gradient waveform as the first FID, so that the image reconstruction uses the same algorithm and compensation function as that for the first FID.

Phantom Experiment: To demonstrate the geometric distortion and motion-related artifacts, UTE and 3D GRE were applied to a phantom filled with 0.1 mM $MnCl_2$/water solution (~ 0.9 s T_1 and ~ 80 ms T_2) with a cylindrical aluminum rod with 4 mm diameter and two plastic hollowed tubings. The phantom was positioned such that the aluminum rod and plastic tubings are positioned perpendicularly to the external magnetic field. UTE data was acquired using imaging parameters of 65,536 radial spokes with undersampling factor 1/3.14, 256 × 256 × 256 mm^3 FOV, readout matrix of 256 oversampled to 512, 1,149 Hz/px receiver bandwidth, TEs of 0.07 and 2.57 ms, TR of 3.6 ms, and 4 sec dummy RF pulses. We constructed another phantom filled with a corn starch jell with 0.1 mM $MnCl_2$/water solution, aluminum rod, a vial of a high-concentration 0.25 mM Gd-DTPA/water solution, and numerous air bubbles. The similar imaging parameters were used for 3D GRE with similar data acquisition time to UTE imaging for both phantoms. Because the phantom experiment would not have any motion other than the table vibration, these data are used to evaluate the motion-effect on the images.

***In-vivo* Experiment:** UTE data for human brain was acquired using imaging parameters of 65,536 radial spokes, 256 × 256 × 256 mm^3 FOV, readout matrix of 256 with 512 oversampled points, 1,149 Hz/px receiver bandwidth, TEs of 0.07 and 2.57 ms, TR of 3.6 ms, and 4 sec dummy RF pulses. UTE data for abdomen was acquired using the following imaging parameters: 131,072 spokes with undersampling factor 1/2.45, 320 × 320 × 320 mm^3 FOV, readout matrix of 320 oversampled to 640 from k_0 = 0, 1,149 Hz/px receiver bandwidth, TEs of 0.07 and 2.57 ms, TR of 3.6 ms, and 4 sec dummy RF pulses. The acquisition time was about 8 min. The similar imaging parameters were used for 3D GRE with similar data acquisition time. 3D UTE phase mapping protocol was applied to a patient with chronic renal failure and kidney dialysis, who is taking a large dose of iron supplement.

Comparison between Local Phase and T_2*: UTE sequence was applied to obtain data for T_2* mapping with TEs = 0.07, 2.07, and 4.07 ms, TR of 5.08 ms, RO matrix of 256 oversampled to 512 from k_0 = 0, 256 × 256 × 256 mm^3 FOV,

65,536 radial spokes for brain, and RO matrix of 320, 320 × 320 × 320 mm^3 FOV, 131,072 radial spokes for abdomen, respectively. Two FIDs with TE 0.07 and 4.07 ms were used for fieldmap calculation, while all three FIDs were used for T_2* mapping by pixel-by-pixel fitting of the signal intensity to a single exponential function $SI(TE) = S_0 e^{-TE/T_2^*}$.

Image Reconstruction of UTE Data: Image reconstruction of the 3D radial data requires either 3D backprojection or regridding of the radial data onto the Cartesian k-space data. Because 3D backprojection may take unacceptably long computation time, the regridding is generally preferred.

We developed an image reconstruction software, the reconstruction software with a user-friendly Graphic-User-Interface (GUI) front-end, using C++ and Anaconda Python package (Continuum Analytics, Austin, TX, USA), which is specially packaged for science and engineering application. GUI was programmed using TkInter, which provides various widgets, including Label, Button, CheckButton, OptionMenu, ListMenu, Entry, Slider, MessageBox, and RadioButton, as shown in Figure 3. Numpy (24) and Scipy (25) packages are heavily used for all array processing.

The matplotlib (21) and pyqtgraph (http://www.pyqtgraph.org) are used for plotting and displaying data in current software. Reslicing of a 3D volume data is performed using the pyqtgraph. The software runs under Linux and Mac OS with appropriate binary file for regridding. Threaded processing is used when possible, particularly during the regridding and Fourier-transformation. The regridding is programmed using C++, following the detailed instruction in Ch. 13.2 of Bernstein's book (6) and compiled to generate a shared object for unix OS (Linux and MacOS). The Kaiser-Bessel regridding kernel is used with the window width 3.0 and $\beta = 4.205$ (28-30). The python package "ctypes" is used to load and pass the pointers of the input and output data between the Python and the regridding function, which is written in C++. To speed up the process, a multi-threaded processing is utilized for regridding and Fourier-Transformation. The software is capable of applying density compensated function (dcf) using a ρ-filter $f(k_r) = k_r^2$ with either a γ-variate function $f(k_r) = k_r^a e^{-k_r/b}$ or a constant value k_{FT}^2 after a specific k_{FT} ($k_r \geq k_{FT}$) (28). The software also suggests the target reconstruction matrix to match the FOV to the acquired radial data by calculating $n_{rc} = k_r^{max}/\Delta k_r$ for a given number of data points.

Reconstruction of 3D radial MRI, particularly using multi-channel receive-only RF coil with a large number of radial spokes, produces a raw data with large size, which requires a computer with large memory. Therefore, these intermediate data objects and all acquisition and reconstruction parameters, which can selectively include unprocessed radial and regridded Cartesian k-space data, and image data, are saved to a local harddisk drive using the package "pickle". Thirty-two bit floating-point is used to reduce the memory usage, instead of the default sixty-four bit in Python. Constructed images, including magnitude and phase images, can be saved to a local harddisk drive in DICOM format using pydicom module (http://www.pydicom.org).

RESULTS

Figure 4(a, b) and 4(c, d) are magnitude and local phase images of UTE and 3D GRE, respectively. Figure 4b looks

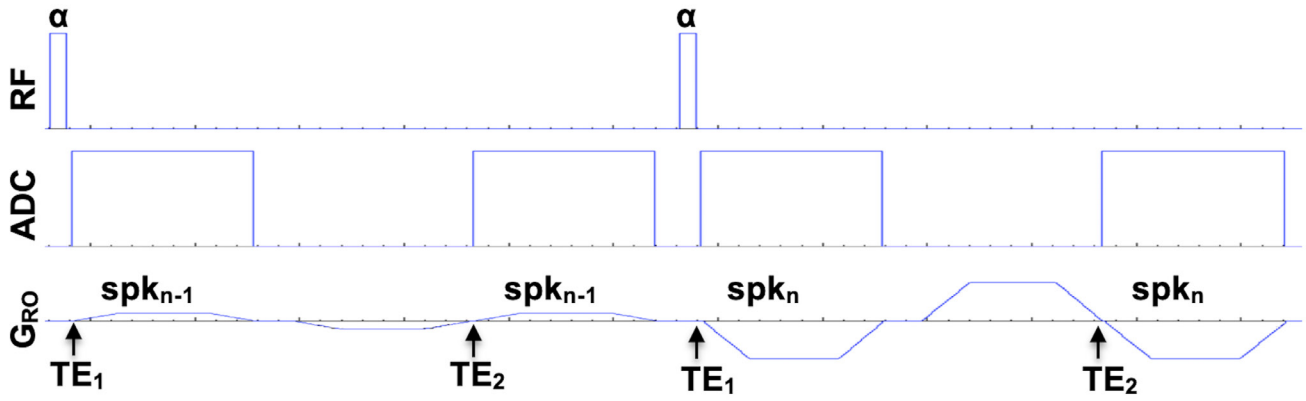

Fig. 2. Pulse sequence diagram for a double FID acquisition. The smooth-varying spoke order is randomly shuffled so that the current readout gradient (spk_n) plays as a spoiling gradient for the previous spoke (spk_{n-1}). The flip angle is set to an Ernst angle for the T_1 of the tissue of our interest.

very much like the simulated phase map in Figure 1d for a cylindrical object, while GRE field map in Figure 4d resemble the distorted simulated images in Figure 1h. Also, motion-related ghosting artifact is visible in 3D GRE magnitude and phase images, which may have been induced by a table vibration during the acquisition.

Images in Figure 5 illustrate the local field distributions of multiple spherical air bubbles, which are caught in the corn starch jell. Field distribution in Figure 5a, for instance those pointed by arrows, mimic exactly the shape in the simulated field maps in Figure 1a. However, those in Figure 5b of the Cartesian sampling mimic the distorted field maps in Figure 1e. On these uniform phantom images, the fraction of the standard deviation with respect to the mean value of an ROI R1 may represent the the degree of the motion artifact. The steDev/mean was measured as 6.2% and 1.5% for the ROI R1 in the Figure 4a and 4c, respectively.

The *in-vivo* brain and abdomen data were used to compare the local phase map with T_2* map. The local phase or field maps in Figure 6 (a, c) illustrate very uniform variation across the brain, kidney, and liver. We don't expect any significant variation in local field in healthy brain and abdomen, as shown in Figure 6a and 6c, respectively. There is large field variation all around the brain tissue in T_2* map in Figure 6b, particularly at frontal lobe due to the air in the sinus, also upper part of the liver as in Figure 6d.

Figure 7a and 7b represent the local phase and QSM images, respectively, which are constructed using the UTE

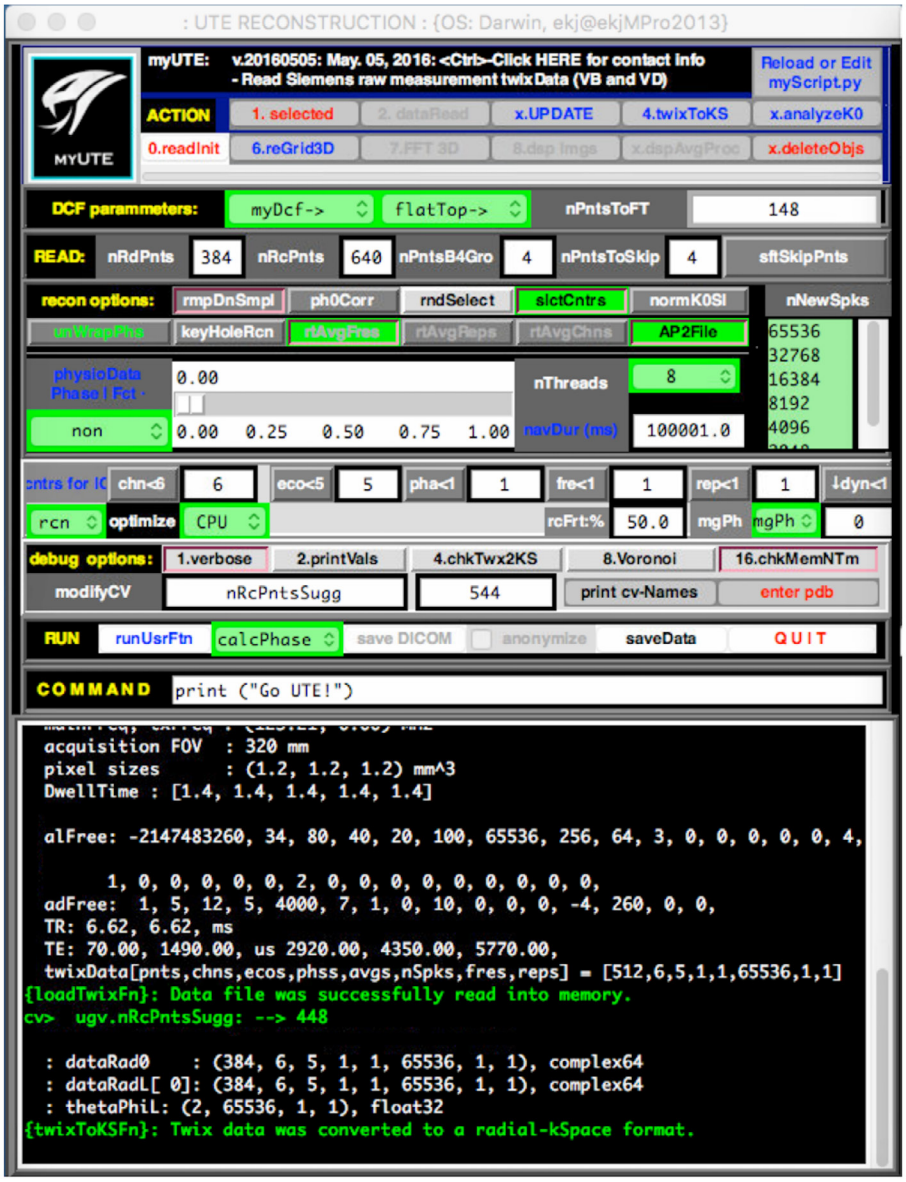

Fig. 3. Front-end of GUI-based reconstruction software. The software is very flexible to set the reconstruction as well as the acquisition parameters. It can selectively reconstruct specific loop counters, such as receive channels, echoes, and repetitions. The current software is capable to reconstruct the UTE raw data from Siemens MRI system with VB and VD version.

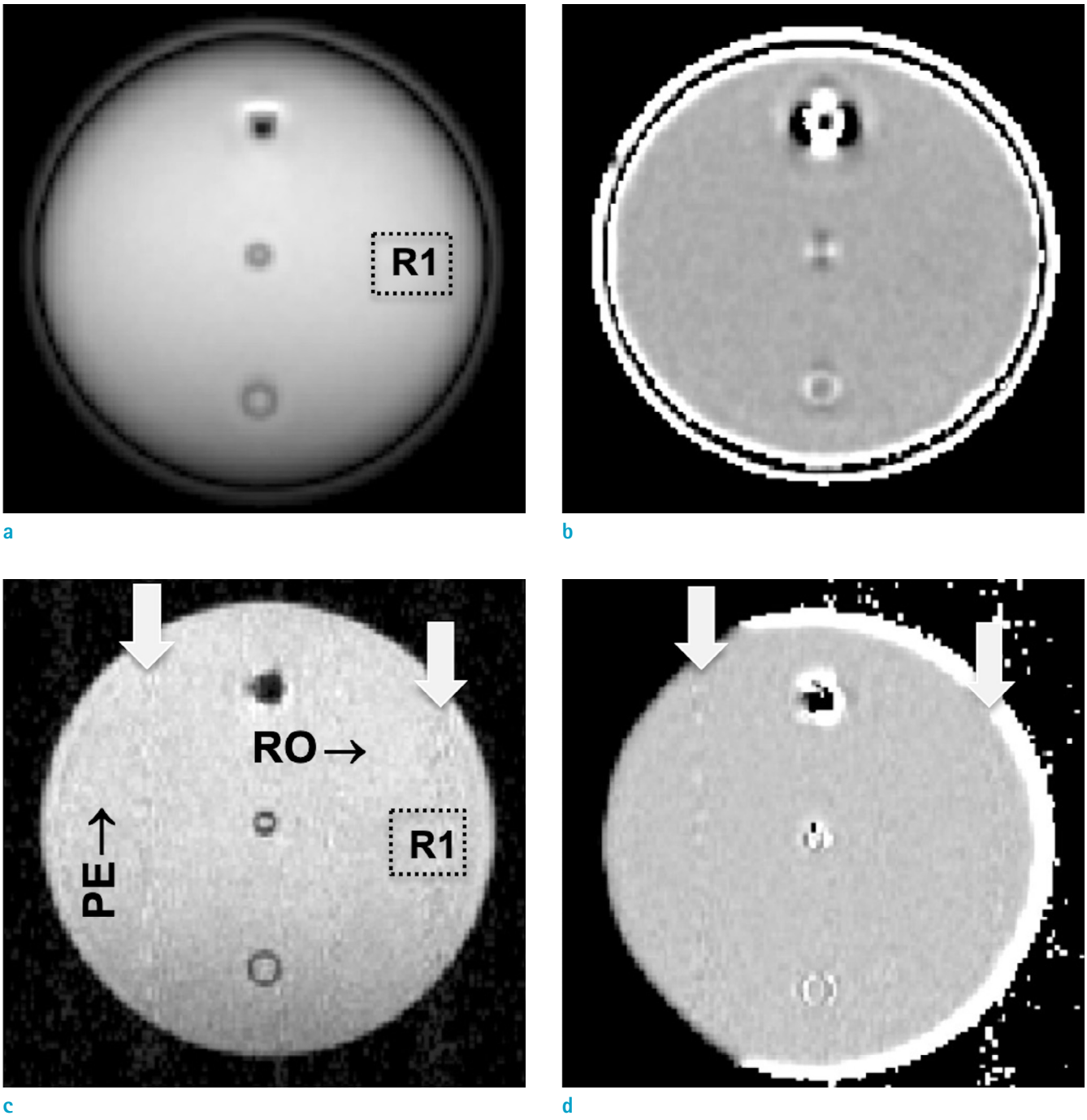

Fig. 4. Magnitude and phase images of (a, b: top row) UTE with TE = 0.07 and 2.07 ms, and (c, d: bottom row) 3D GRE with TE = 1.6 and 3.6 ms on a phantom filled with MnCl2/water solution and aluminum and two plastic tubings from top to bottom. Note the distorted and asymmetric magnitude and phase images around the aluminum rod and motion-artifact in GRE images in (c, d), indicated by downward arrows.

data with TE 0.07 and 2.57 ms. With low threshold value of F_{th} = 2.0, susceptibility image clearly resembles the local phase map, except for streaking artifacts.

The local field maps of the kidney patient are illustrated in Figure 8. Mean values of selected regions-of-interest (ROIs) on various organs were measured on the local field maps. Note that the volume magnetic susceptibility of pure water and fatty phospholipid are -9.035 and -9.68 ppm (31),

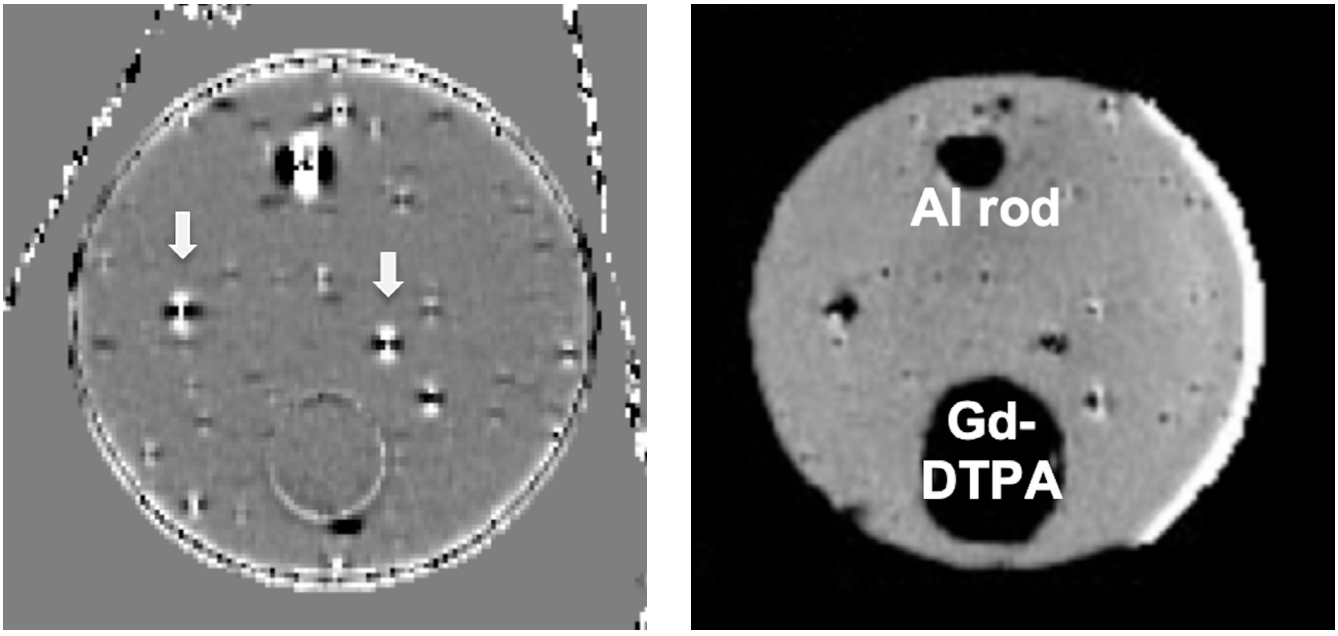

a b

Fig. 5. Local phase images of a phantom filled with corn starch gel with aluminum rod, a vial filled with high-concentration Gd-DTPA solution, multiple spherical air bubbles, measured using (a: Lt) UTE and (b: Rt) 3D GRE. Note that all local phases are symmetric in UTE phase maps as pointed by arrows, while they mimic the distorted images in Figure 1.

respectively, which are very close to each other. Therefore, local field at fat must be dominated by the chemical shift difference from the water proton. The field difference of the fat proton from the water proton due to the chemical shift differences (-4.7 and -1.2 ppm) is +3.5 ppm, which can be used as an internal reference. Therefore, these numbers represent the relative field to the pure water proton at -4.7 ppm. As presented in the Table 1, local field tends to be increased in the patient's organs compared with those in the healthy subject, as if the paramagnetic irons are accumulated. Further investigation is needed on increased numbers of healthy and patient subjects.

DISCUSSION

Unlike in the phase images that are calculated from the data acquired using the conventional FTMRI, such as using 3D GRE, of which geometrical distortion is obvious toward the readout direction as shown in Figure 4d for a cylinder and Figure 5b for a spherical object, phase images in Figures 4b and 5a using UTE clearly mimic the simulated local field images in Figure 1 for cylinder and sphere, respectively. This is because the readout direction of the UTE MRI is uniformly distributed toward the entire spherical surface. Although these true phase map may be generated from the GRE phase image using specific algorithm, such as SHARP (32), UTE produces true field map without any further post processing.

Another notable advantage of radial UTE over GRE is its immunity to the motion-induced artifact, which is common to all conventional MRI using phase-encoding. The error is induced into the signal phase by physiological motion coupled with phase-encoding gradient. Because UTE is projection imaging technique with heavy sampling of the ko data, no motion-induced ghost artifact is expected. The motion artifact in Figure 4 (c, d) was induced by the convective motion in the fluid by the table vibration due to switching imaging gradients. This feature is particularly important for application to abdomen imaging, which usually requires multiple breathold acquisitions.

One major issue with 3D radial MRI is a difficulty to reconstruct the data, particularly for data measured with a large number of radial spokes and multiple receivers. Reconstruction of this type of raw data requires a computer with a very large memory, particularly using interpreting languages, such as Python and Matlab (Mathworks Inc., Natick, MA), which are known with poor memory

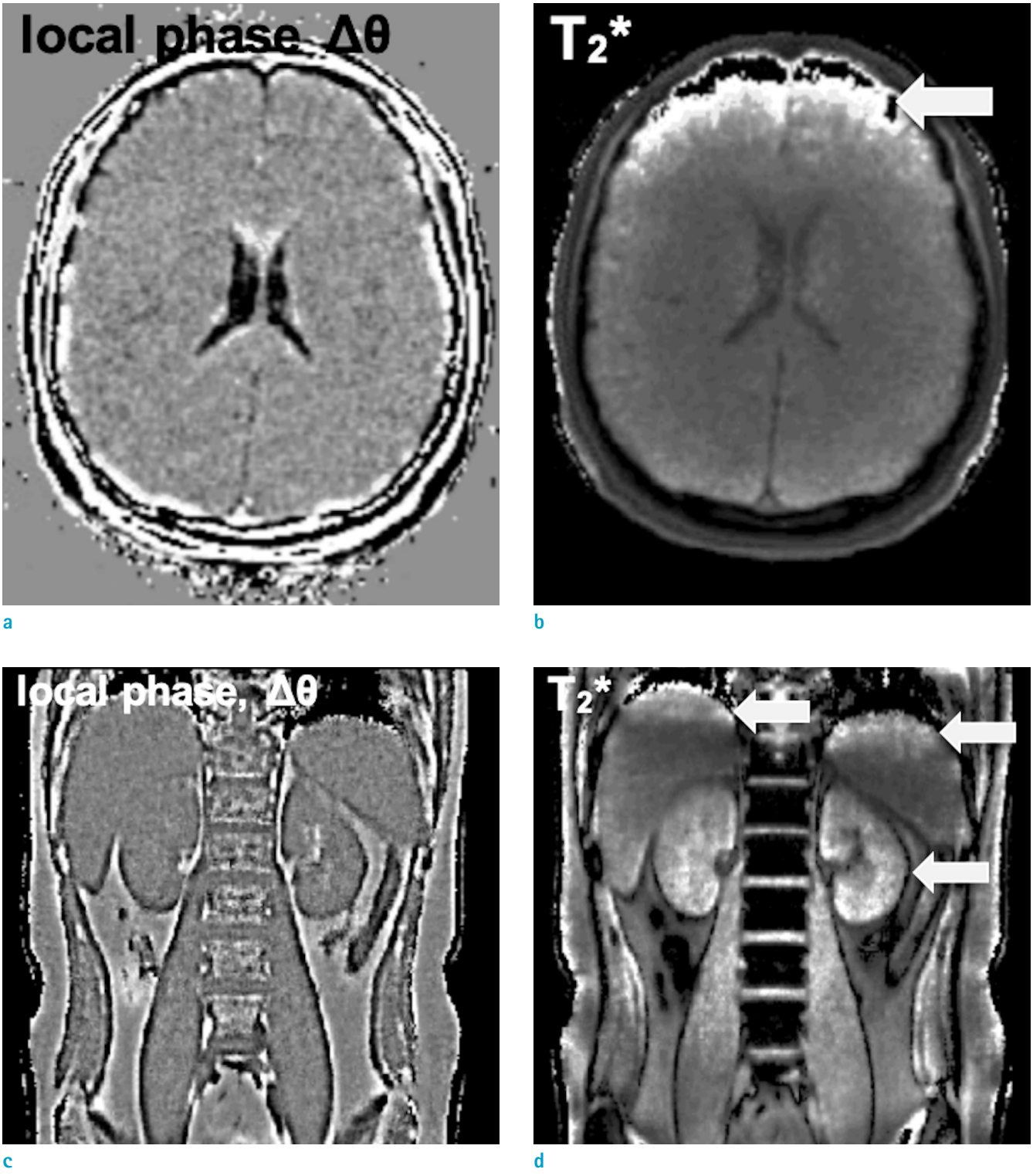

Fig. 6. (a, c: first and third columns) Local phase maps, and (b, d: second and forth columns) T_2* maps of *in-vivo* brain and abdomen of a healthy volunteer. The same data set with TE = 0.07, 2.07, and 4.07 ms was used for T_2* and TE = 0.07 and 4.07 ms for local phase mappings. Non-uniformity in the T_2* map is clearly visible at the frontal lobe brain (b) and upper part of liver close to lung space and kidney (d).

management. For instance, the size of the raw data for 320 readout points oversampled to 640 points, 131,072 spokes, two echoes for phase mapping, and 6 Rx channels exceeds 8.255 GB. It takes 38 min for regridding and 7.5 min for 3D fft on a Mac Pro (2013) with 3.5 GHz hexacore Intel Xeon E5 CPU and 128 GB memory. The complexity in constructing images of UTE data with a large number of spokes, multiple Rx channel, and multiple FIDs, may be overcome by utilizing

Table 1. Magnetic Susceptibility Values in ppm with Respect to Pure Water Proton at –4.7 ppm, Measured in Various Abdominal Organs of a Healthy and Dialysis Patient with Renal Failure

Organ	Liver	Kidney parenchyma	Pancreas	Muscle	Intervertebral disc	Fat	Pure water
Healthy	-1.99	-1.98	-0.64	-0.78	-2.61	3.50	0
Patient	0.79	-1.91	-0.25	-1.11	-1.35	3.50	0

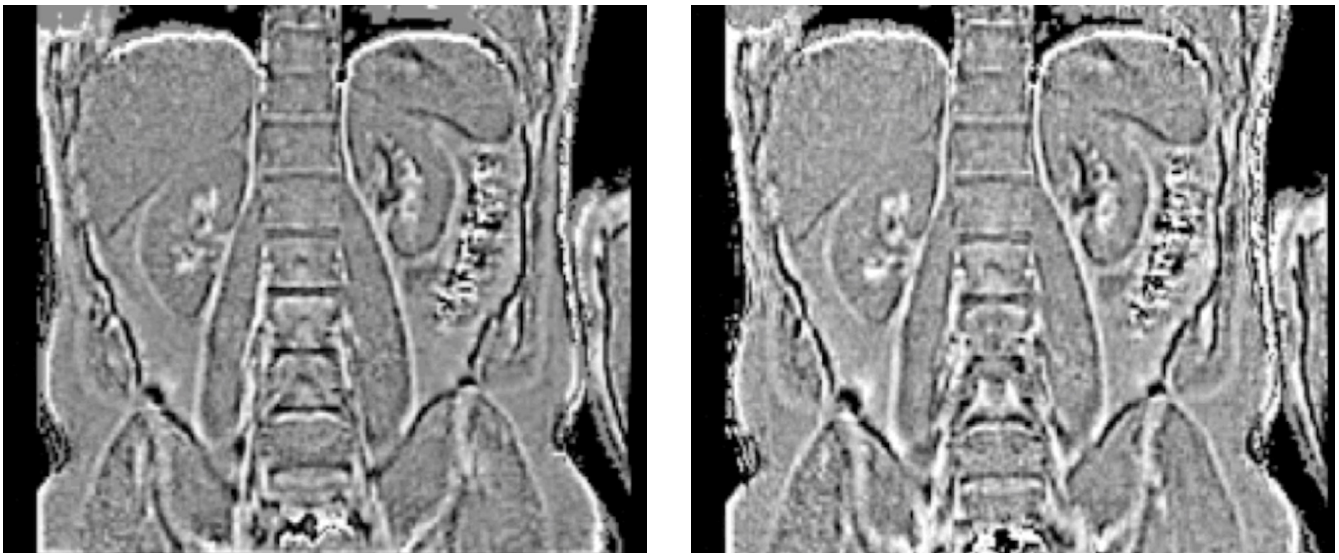

a b

Fig. 7. (a: Lt) Local phase and (b: Rt) QSM maps of abdomen from a healthy volunteer using UTE with nSpks = 131,072, TR = 3.60 ms, TE = 0.070, 2.57 ms, 1 mm^3, $\alpha = 4.5°$. QSM map was calculated using the FT method with $F_{th} = 2$.

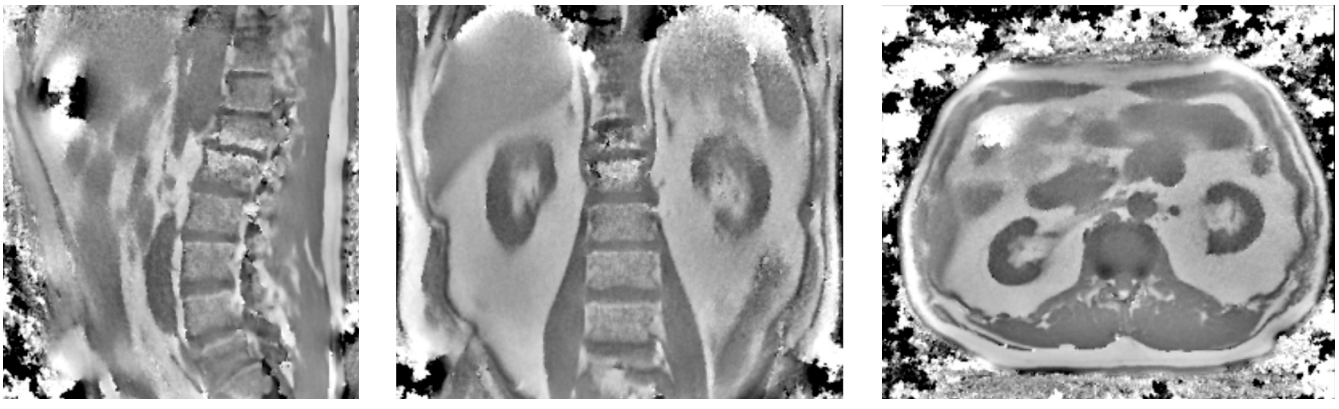

a b c

Fig. 8. Local field maps of a kidney dialysis patient in (a: Lt) sagittal, (b: Mid) coronal, (c: Rt) axial planes.

the effective reconstruction algorithm, such as using accelerated processing with GPU and/or message-passing interface (MPI) with increased threads or Linux cluster.

Although the phase mapping using UTE is not popular, mainly because of complexity of image reconstruction, it has been used successfully for QSM by Xie (16) for a dynamic contrast imaging. Gho et.al. used UTE phase image to map the QSM of the brain, but unfortunately minimal detail is presented in the report (17) for QSM. For a routine use of local phase mapping using UTE, two TEs may be chosen to be TE_{min} and TE_{min}+ 2.5 ms, with minimum TR to maximize the number of radial spokes. Although increased ΔTE may produce field-map with reduced noise, it will significantly increase the acquisition time. In our preliminary experience with phase mapping of human abdomen, we recommend at least 131,072 spokes for 320 readout matrix, maximum receiver bandwidth, and 320 mm or larger FOV. Respiratory gating may help reducing the blurring on the resultant UTE images, however, it will add a significant amount of time to already long data acquisition time. Fortunately, our preliminary results indicate that UTE images with free-breathing acquisition provides decent abdominal images, as shown in Figure 7.

Another major advantage of UTE over GRE is its significantly reduced susceptibility artifact size at/near the interfaces between the tissue and air, bone or foreign object. The artifact size is approximately equal to $\Delta\chi B_o T_E$/BW (33). With shorter TE, the artifact size can be reduced. Hence, UTE can be used with TE_{min} and another short TE for phase-mapping of large field variation, where GRE imaging will fail to detects any signal and result in image with large signal void.

After removing the background phase, one can obtain local field image, which is induced by purely the local tissue susceptibility distribution. T_2* mapping has long been used to estimate the local field variation. The measured relaxation rate $1/T_2$* is a sum of multiple terms as $R_2^* = \frac{1}{T_2^*} = \frac{1}{T_2} + \frac{1}{2T_1} + \gamma\Delta B_z$ where $\gamma\Delta B_z$ is a sum of global and local field distribution, as $\gamma\Delta B_z = \gamma\Delta B_z^G + \gamma\Delta B_z^L$ (5-8). For instance, T_2* was reported as about 10 ~ 20 ms for normal liver (34, 35). These values are translated to R_2* = 50 ~ 100 sec^{-1}. In clinical MRI of tissue water at the field strength 1.0 ~ 3.0 T, the spin-lattice and spin-spin relaxation times are in the order of 1.0 and 0.1 sec, respectively. Thus, $1/2T_1 < 1.0$ sec^{-1}, $1/T_2 = \sim 10$ sec^{-1}, therefore, R_2* is dominated by the field inhomogeneity term $\gamma\Delta B_z$. If the background field variation is large, T_2* value represent the background field ΔBz at specific location, as indicated by arrows in Figure 6b and 6d. We don't anticipate that there would be any visible or measurable difference in local field, as indicated in the T_2* map in Figure 6d. Note that the local field images in Figure 6a and 6c, which are calculated using UTE, are very uniform, unlike their counter T_2* maps in Figure 6b and 6d. Our preliminary susceptibility maps, shown in Figures 7b and 8, is to demonstrate for more advanced quantitative analysis using UTE phase image. These local field and susceptibility maps may be used for quantitative measurements of kidney physiology.

The disadvantage of 3D radial acquisition is that a large number of readout data is required to fulfill the Nyquist sampling theorem in the outer k-space, say $N_\theta^{Nyq} = \pi N_r^2$ for a Nyquist-fulfilled 3D UTE, i.e., half-spoke radial sampling, where N_θ and N_r indicate the number of samples in angular and radial directions, respectively. This leads to an increase of data acquisition time and data size. However, because ultra-short TE can more effectively be incorporated with center-out radial sampling requiring no readout prephasing and phase-encoding gradients, time of each readout is shorter than that of a Cartesian sampling scheme. Therefore, radial UTE will have shorter TR even with higher number of readouts. Although the images in current work don't show visible streaking artifact, probably because of large number of radial spokes, the artifact may be spreaded on the resultant images. Further additional correction, such as the trajectory error correction (36, 37), may be performed to improve the image quality.

CONCLUSIONS

We successfully produced the phase image with free of motion-artifact and greatly reduced geometric distortion using UTE MRI. Because the reconstruction process of UTE data requires several complex processes for each loop counters, such as radial spoke, receiver channel, and echo, which include resampling of radial k-space data to Cartesian k-space grid and 3D fft, the reconstruction of UTE data with multiple receiver channel and large number of radial spokes is very time-consuming. It also requires a high-end computer with large memory (≥ 64 GB). These motion- and distortion-free phase map can be used to produce local tissue field map, which may be useful to evaluate the change in magnetic property in the human body, such as iron overloading in brain and abdominal organs.

REFERENCES

1. Haacke EM, Mittal S, Wu Z, Neelavalli J, Cheng YC. Susceptibility-weighted imaging: technical aspects and clinical applications, part 1. AJNR Am J Neuroradiol 2009;30:19-30
2. Mittal S, Wu Z, Neelavalli J, Haacke EM. Susceptibility-weighted imaging: technical aspects and clinical applications, part 2. AJNR Am J Neuroradiol 2009;30:232-252
3. Shmueli K, de Zwart JA, van Gelderen P, Li TQ, Dodd SJ, Duyn JH. Magnetic susceptibility mapping of brain tissue in vivo using MRI phase data. Magn Reson Med 2009;62:1510-1522
4. Schweser F, Deistung A, Sommer K, Reichenbach JR. Toward online reconstruction of quantitative susceptibility maps: superfast dipole inversion. Magn Reson Med 2013;69:1582-1594
5. Haacke EM, Brown RW, Thompson MR. Magnetic resonance imaging, physical principles and sequence design. New York, NY: Wiley-Liss, 1999
6. Zhou XJ, Bernstein MA, King KF. Handbook of MRI pulse sequences. New York, NY: Elsevier Science, 2005
7. Slichter CP. Principles of magnetic resonance. 3rd ed. Berlin, Heidelberg, New York: Springer-Verlag, 1990
8. Fukushima E, Roeder SBW. Experimental pulse NMR: A nuts and bolts approach. Reading, MA: Addison-Wesley Publishing Company, Inc., 1981
9. Sharma SD, Hernando D, Horng DE, Reeder SB. Quantitative susceptibility mapping in the abdomen as an imaging biomarker of hepatic iron overload. Magn Reson Med 2015;74:673-683
10. Barrera Portillo MC, Uranga Uranga M, Sanchez Gonzalez J, Alustiza Echeverria JM, Gervas Wells C, Guisasola Iniguez A. Liver and heart T2* measurement in secondary haemochromatosis. Radiologia 2013;55:331-339
11. Li W, Wu B, Liu C. Quantitative susceptibility mapping of human brain reflects spatial variation in tissue composition. Neuroimage 2011;55:1645-1656
12. He X, Yablonskiy DA. Biophysical mechanisms of phase contrast in gradient echo MRI. Proc Natl Acad Sci U S A 2009;106:13558-13563
13. Yablonskiy DA, Luo J, Sukstanskii AL, Iyer A, Cross AH. Biophysical mechanisms of MRI signal frequency contrast in multiple sclerosis. Proc Natl Acad Sci U S A 2012;109:14212-14217
14. Jeong EK, Kim SE, Guo J, Kholmovski EG, Parker DL. High-resolution DTI with 2D interleaved multislice reduced FOV single-shot diffusion-weighted EPI (2D ss-rFOV-DWEPI). Magn Reson Med 2005;54:1575-1579
15. He Q, Ma Y, Fan S, et al. Direct magnitude and phase imaging of myelin using ultrashort echo time (UTE) pulse sequences: a feasibility study. Magn Reson Imaging 2017;39:194-199
16. Xie L, Layton AT, Wang N, et al. Dynamic contrast-enhanced quantitative susceptibility mapping with ultrashort echo time MRI for evaluating renal function. Am J Physiol Renal Physiol 2016;310:F174-F182
17. Gho SM, Shin J, Kim MO, Kim DH. Simultaneous quantitative mapping of conductivity and susceptibility using a double-echo ultrashort echo time sequence: Example using a hematoma evolution study. Magn Reson Med 2016;76:214-221
18. Jackson JD. Classical electrodynamics. 2nd ed. New York: Wiley, 1975
19. Griffiths DJ, Introduction to electrodynamics. 4th ed. Pearson, 2012
20. Case TA, Durney CH, Ailion DC, Cutillo AG, Morris AH. A mathematical model of diamagnetic line broadening in lung tissue and similar heterogeneous systems: calculations and measurements. J Magn Reson 1987;73:304-314
21. Salomir R, De Senneville BD, Moonen CTW. A fast calculation method for magnetic field inhomogeneity due to an arbitrary distribution of bulk susceptibility. Concepts Magn Reson Part B Magn Reson Eng 2003;19:26-34
22. Abdul-Rahman HS, Gdeisat MA, Burton DR, Lalor MJ, Lilley F, Moore CJ. Fast and robust three-dimensional best path phase unwrapping algorithm. Appl Opt 2007;46:6623-6635
23. Robinson S, Grabner G, Witoszynskyj S, Trattnig S. Combining phase images from multi-channel RF coils using 3D phase offset maps derived from a dual-echo scan. Magn Reson Med 2011;65:1638-1648
24. van der Walt S, Colbert SC, Varoquaux G. The NumPy array: a structure for efficient numerical computation. Comput Sci Eng 2011;13:22-30
25. Oliphant TE. SciPy: Open source scientific tools for Python. Comput Sci Eng 2007;9:10-20
26. Hunter JD. Matplotlib: A 2D graphics environment. Comput Sci Eng 2007;9:99-104
27. Hunter JD. Matplotlib: A 2D graphic environment. Comput Sci Eng 2007;9:90-95
28. Nielles-Vallespin S, Weber MA, Bock M, et al. 3D radial projection technique with ultrashort echo times for sodium MRI: clinical applications in human brain and skeletal muscle. Magn Reson Med 2007;57:74-81
29. Jackson JI, Meyer CH, Nishimura DG, Macovski A. Selection of a convolution function for Fourier inversion using gridding [computerised tomography application]. IEEE Trans Med Imaging 1991;10:473-478
30. Johnson KO, Pipe JG. Convolution kernel design and

efficient algorithm for sampling density correction. Magn Reson Med 2009;61:439-447
31. Liu C, Li W, Tong KA, Yeom KW, Kuzminski S. Susceptibility-weighted imaging and quantitative susceptibility mapping in the brain. J Magn Reson Imaging 2015;42:23-41
32. Schweser F, Deistung A, Lehr BW, Reichenbach JR. Quantitative imaging of intrinsic magnetic tissue properties using MRI signal phase: an approach to in vivo brain iron metabolism? Neuroimage 2011;54:2789-2807
33. Schenck JF. The role of magnetic susceptibility in magnetic resonance imaging: MRI magnetic compatibility of the first and second kinds. Med Phys 1996;23:815-850
34. Yu H, McKenzie CA, Shimakawa A, et al. Multiecho reconstruction for simultaneous water-fat decomposition and T2* estimation. J Magn Reson Imaging 2007;26:1153-1161
35. Yu H, Shimakawa A, McKenzie CA, Brodsky E, Brittain JH, Reeder SB. Multiecho water-fat separation and simultaneous R2* estimation with multifrequency fat spectrum modeling. Magn Reson Med 2008;60:1122-1134
36. Speier P, Trautwein F. A calibration for radial imaging with large inplane shifts. In Proceedings of the 13th Annual Meeting of ISMRM, Miami Beach, Florida, USA, 2005:2295
37. Speier P, Trautwein F. Robust radial imaging with predetermined isotropic gradient delay correction. In Proceedings of the 14th Annual Meeting of ISMRM, Seattle, Washington, USA, 2006:2379